Topology, Geometry, and Mechanics of Strongly Stretched and Twisted Filaments: Solenoids, Plectonemes, and Artificial Muscle Fibers

Nicholas Charles,[1] Mattia Gazzola,[2] and L. Mahadevan[3,4,*]

[1]*Paulson School of Engineering and Applied Sciences, Harvard University, Cambridge, Massachusetts 02138, USA*
[2]*Department of Mechanical Science and Engineering and National Center for Supercomputing Applications,
University of Illinois at Urbana-Champaign, Urbana, Illinois 61801, USA*
[3]*Paulson School of Engineering and Applied Sciences, Department of Physics, Department of Organismic and Evolutionary Biology,
Harvard University, Cambridge, Massachusetts 02138, USA*
[4]*Kavli Institute for Nanobio Science and Technology, Harvard University, Cambridge, Massachusetts 02138, USA*

Soft elastic filaments that can be stretched, bent, and twisted exhibit a range of topologically and geometrically complex morphologies. Recently, a number of experiments have shown how to use these building blocks to create filament-based artificial muscles that use the conversion of writhe to extension or contraction, exposing the connection between topology, geometry, and mechanics. Here, we combine numerical simulations of soft elastic filaments that account for geometric nonlinearities and self-contact to map out the basic structures underlying artificial muscle fibers in a phase diagram that is a function of the extension and twist density. We then use ideas from computational topology to track the interconversion of link, twist, and writhe in these geometrically complex physical structures to explain the physical principles underlying artificial muscle fibers and provide guidelines for their design.

The bending and twisting elastic response of soft filamentous objects is a consequence of the separation of scales inherent in their slender geometries. This realization is at the heart of the classical Kirchhoff-Love theory [1,2], which considers inextensible, unshearable filaments and has spawned substantial literature [3,4]. When such filaments are twisted strongly, they deform into plectonemic structures that consist of self-braided segments and which have been observed across scales, from DNA to metal wires [5,6]. The transition between the straight and plectonemic structures in inextensible filaments has been explored extensively in both a deterministic and a stochastic setting [7–10] and continues to be a topic of interest. However, filaments made of soft elastomeric materials are also easily extensible and shearable, and their study is interesting for a range of applications such as biological tissue mechanics, soft robotics, etc [11]. Among the simplest behaviors that harnesses these modes of deformation is the controlled transition between straight filaments and tightly coiled helical shapes (solenoids) originally observed in textiles [12], quantified experimentally in elastomers [13], and then rediscovered in the context of heat-driven artificial muscles [14]. These energy-harvesting devices rely on the conversion of twist and bend into extension [15–17], as solenoids untwist and stretch. Here we consider the interplay between topology, geometry, and mechanics in strongly stretched and twisted filaments and their functional consequences.

We describe a filament by a centerline position vector $\bar{x}(s, t) \in \mathbb{R}^3$ ($s \in [0, L_0]$ is the material coordinate of the rod of rest length L_0 at time t), while the orientation of its cross section is defined by an initially orthonormal triad associated with the director vectors $\bar{d}_i(s, t), i = 1, 2, 3$, where $\bar{d}_3(s, t)$ is normal to the material cross section of the filament. Then, the transformation of the body-fixed frame (quantities without overbar) to the lab-fixed frame (quantities with overbar) can be written in terms of the rotation matrix $Q(s, t) = \{\bar{d}_1, \bar{d}_2, \bar{d}_3\}^{-1}$ [see Fig. 1(a)].

In general, the centerline tangent $\partial_s \bar{x} = \bar{x}_s$ does not point along the normal to the cross section $\bar{d}_3(s, t)$. The deviation between these vectors characterizes local extension and shear $\sigma = Q(\bar{x}_s - \bar{d}_3) = Q\bar{x}_s - d_3$ [Fig. 1(a)] and is the basis of the Cosserat rod theory [3] that allows us to include all six modes of deformation at every cross section [mathematically, this is associated with the dynamics on the full Euclidean group SE(3)]. The restriction to the Kirchhoff theory corresponds to the case $\sigma = 0$; i.e., the normal to the cross section is also the tangent to the centerline, with $\bar{x}_s - d_3 = 0$.

Since many soft materials are close to being incompressible (i.e., the shear modulus is much smaller than the bulk modulus), filaments made of such materials will also be incompressible. Then, if $e = |\bar{x}_s|$ is the local elongation factor and A is the local cross-sectional area, Ae is constant locally. Accounting for this nonlinear constraint along with a simple materially linear constitutive law provides is a reasonable approximation to both neo-Hookean and Mooney-Rivlin materials (see Ref. [18] and
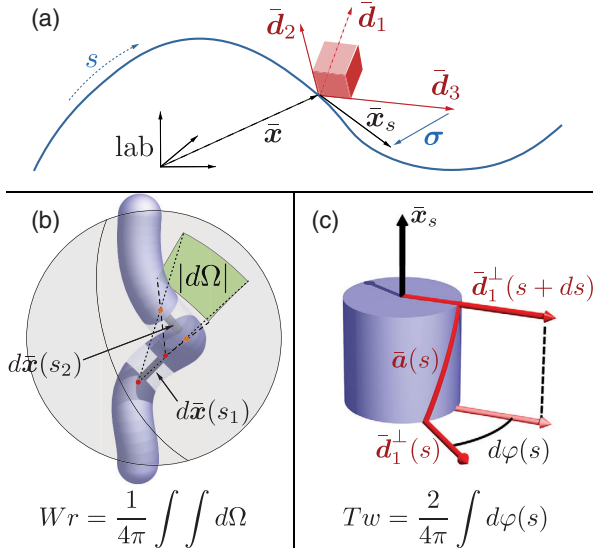
FIG. 1. Geometry and topology of soft extensible filaments. (a) The filament centerline $\bar{x}(s, t)$ and local orthogonal frame $\{\bar{d}_1, \bar{d}_2, \bar{d}_3\}$. Shear and extension are defined by the vector $\boldsymbol{\sigma} = \boldsymbol{Q}\bar{x}_s - \boldsymbol{d}_3$, while curvature and twist are defined by the vector $\mathbf{k} = \text{vec}(\boldsymbol{Q}'\boldsymbol{Q}^{\mathrm{T}})$. (b) Writhe (Wr) equals the centerline's average oriented self-crossing number computed in terms of the integral of the solid angle $d\Omega$ determined by the infinitesimal centerline segments $\bar{x}(s_1)$ and $\bar{x}(s_2)$ (left-handed intersections are negative). (c) Twist (Tw) is the integral of the infinitesimal rotations $d\varphi$ of the auxiliary curve $\bar{a}$ around $\bar{x}_s$. Here, the vector $\bar{a}$ traced out by $\bar{d}_1^{\perp}$ (i.e., the projection of $\bar{d}_1$ onto the normal-binormal plane) is shown in red while the curve associated with $-\bar{d}_1$ is shown in yellow (see Fig. 2). For a closed curve Lk = Tw + Wr, where Lk (link) is the average oriented crossing number of $\bar{x}(s)$ with $\bar{a}(s)$.

the Supplemental Material [19] for model validation and more details about the physical model and numerical scheme, and Refs. [25–27] for alternative approaches).

Then, we may write the linear and angular momentum balance equations as [3,4,18]

$$\rho A \cdot \partial_t^2 \bar{x} = \partial_s \left(\frac{\boldsymbol{Q}^T \boldsymbol{S} \boldsymbol{\sigma}}{e} \right) + e\bar{f}$$

$$\frac{\rho \boldsymbol{I}}{e} \cdot \partial_t \boldsymbol{\omega} = \partial_s \left(\frac{\boldsymbol{B}\boldsymbol{k}}{e^3} \right) + \frac{\boldsymbol{k} \times \boldsymbol{B}\boldsymbol{k}}{e^3} + \left(\boldsymbol{Q} \frac{\bar{x}_s}{e} \times \boldsymbol{S}\boldsymbol{\sigma} \right)$$
$$+ \left(\rho \boldsymbol{I} \cdot \frac{\boldsymbol{\omega}}{e} \right) \times \boldsymbol{\omega} + \frac{\rho \boldsymbol{I}\boldsymbol{\omega}}{e^2} \cdot \partial_t e + e\boldsymbol{c},$$

where ρ is the material density, $\bar{\boldsymbol{\omega}} = \text{vec}(\partial_t \boldsymbol{Q}^T \boldsymbol{Q})$ is the local angular velocity, $\bar{\boldsymbol{k}} = \text{vec}(\partial_s \boldsymbol{Q}^T \boldsymbol{Q})$ is the local strain vector (of curvatures and twist), $\boldsymbol{S}$ is the matrix of shearing and extensional rigidities, $\boldsymbol{B}$ is the matrix of bending and twisting rigidities, and $\boldsymbol{f}, \boldsymbol{c}$ are the body force density and external couple density (see the Supplemental Material [19] or Ref. [18] for details).

To follow the geometrically nonlinear deformations of the filament described by the equations above, we employ a recent simulation framework [18], wherein the filament is discretized in to a set of $n + 1$ vertices $\{\bar{x}_i\}_{i=0}^n$ connected by edges $\bar{e}^i = \bar{x}_{i+1} - \bar{x}_i$, and a set of n frames $\{\boldsymbol{Q}^i\}_{i=0}^{n-1}$. The resulting discretized system of equations is integrated using an overdamped second-order scheme, reducing the dynamical simulation to a quasistatic process, while accounting for self-contact forces, internal viscous forces, and the dynamic modification of the filament geometry and stiffness (see Supplemental Material [19] and Ref. [18] for details) while ignoring friction.

To track the knotlike structures that form when the stretched and twisted filament can contact itself, we take advantage of the Calugareanu-Fuller-White theorem [28,29]: Lk = Tw + Wr. Here, link is the oriented crossing number (or Gauss linking integral) of the centerline and auxiliary curve $\bar{a}(s)$ (Fig. 1) averaged over all projection directions [30], writhe is the link of the centerline with itself [31], and twist denotes the local rotation of the auxiliary curve about the centerline tangent. In a discrete setting, we compute writhe, link, and twist of the filament modeled as an open ribbon following Ref. [32], as illustrated in Fig. 1 (see the Supplemental Material [19] for details).

When inextensible filaments are stretched and twisted, a range of localized and self-contacting structures arise and have been well studied in both a deterministic and stochastic setting [9,10,33–36]. For highly stretched and twisted filaments, the phase space of possibilities is much richer, and in particular, a new morphological phase associated with tightly coiled helices (solenoids) appears [12,13]. To characterize these morphologies, we simulate twisting a filament clamped at one end and prestretched by a constant axial load. We first use an axial load ∼25 times the critical compressive buckling force of a corresponding inextensible filament $F_C = (\pi^2 EI)/L_0^2$. In Fig. 2(a), denoting by a the filament rest configuration radius, we show that when a critical dimensionless twist density Φa is reached, the filament becomes unstable to bending, leading to the formation of a plectoneme, converting twist to writhe. As the twist is increased further, occasionally the plectoneme can partially untie itself by slipping a loop over an end point, allowing the link to escape the system (see Fig. S3 in the Supplemental Material [19]). In Fig. 2(b), we repeat the simulation but quadruple the stretching strain and see that at a critical value of Φa, the filament again becomes unstable to bending but now leads to a qualitatively different equilibrium configuration: a tightly coiled helical solenoid. We note that substantial prestretch is the crucial prerequisite for solenoid formation, while shearing is found to be unimportant (see Supplemental Material [19] for details). While both plectonemes and solenoids convert twist to writhe in steps, they are otherwise quite different. Plectonemes lead to braids made of oppositely chiral helices, while solenoids lead to a single compact helix.
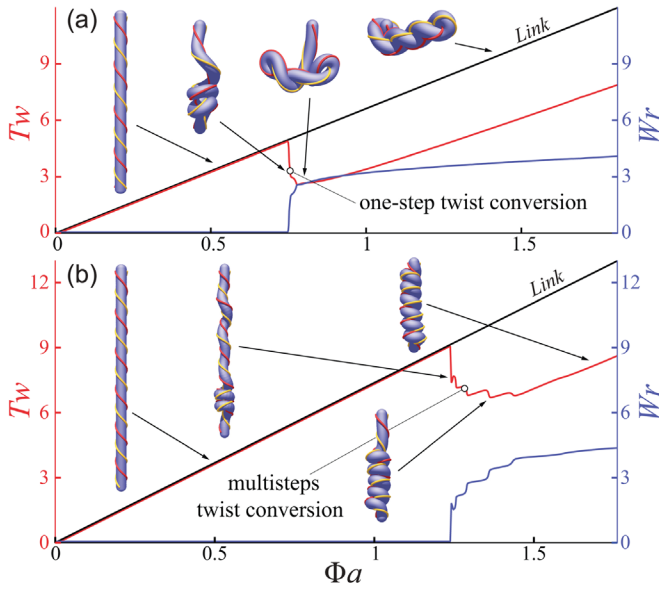
FIG. 2. Variation of the link, twist, and writhe as a function of the dimensionless twist density Φa (a is the filament radius in the rest configuration). (a) To replicate the experimental observations in Ref. [13], we use a constant vertical load $F \approx 25F_C$ to produce a plectoneme ($F_C = \pi^2 EI/L_0^2$ is the buckling force for an inextensible rod; see Video S1 in the Supplemental Material [19] and Ref. [37]). (b) We repeat the simulation with $F \approx 90F_C$, stretching the filament to deformed length $L \approx 1.16L_0$. Increased stretching leads to an overall similar conversion of twist to writhe leading to tightly packed solenoidal structures (see Video S2 and the Supplemental Material [19] for plots of filament energy). Simulation settings (see Supplemental Material [19]): length $L_0 = 1$ m, $a = 0.025L_0$, Young's modulus $E = 1$ MPa, shear modulus $G = 2E/3$, $S = \text{diag}(4GA/3, 4GA/3, EA)$ N, $\mathbf{B} = \text{diag}(EI_1, EI_2, GI_3)$ N m^2.

FIG. 3. Morphological phase space. We simulate a filament prestretched to L/L_0 by a constant axial load and twisted by an angle Φa, as in Fig. 2. By computing centerline relative alignment in neighboring loops, we find four phases: straight, plectoneme, solenoid, and plectoneme-solenoid combinations. Plectoneme alignment ≈ -1, solenoid alignment ≈ 1, and transition configuration alignments approach 0 (dark green). For $L/L_0 \gtrsim 1.1$, solenoids are preferred. We expect Φ_{critical} to scale linearly with L/L_0 at high extension, in agreement with this plot. Our results agree qualitatively with experiments [13] (shown in black dots; see Supplemental Material [19] for details). Hollow symbols denote plectoneme transitions, while solid points denote solenoid transitions; different shapes correspond to different filament parameters (Supplemental Material [19]). Simulation settings (Supplemental Material [19]): $L_0 = 1$ m, $a = 0.025L_0$, $E = 1$ MPa, $G = 2E/3$, $S = \text{diag}(4GA/3, 4GA/3, EA)$ N, $\mathbf{B} = \text{diag}(EI_1, EI_2, GI_3)$ N m^2.

Furthermore, a plectoneme loop converts much more twist to writhe than a solenoid does as it coils up (Fig. 2). However, the tightly coiled nature of the solenoidal coil makes it more stable under stretching.

We now turn to explain the experimental observations and morphological phase diagram that span the twist density-extensional strain $(\Phi a) - (L/L_0)$ phase space [13] (L is the stretched filament length). Using randomly sampled twist densities and extensions in this phase space, we classify each resulting configuration on the spectrum from plectoneme to solenoid using the average relative alignment of tangent vectors at filament segments which are adjoining in absolute coordinates but separated in material coordinates, i.e., $\text{avg}_{i=1}^n [\text{sgn}(\bar{e}^i \cdot \bar{e}^k)]$, where $k = \text{argmin}(|\bar{x}_k - \bar{x}_i|)$ subject to $|k - i| > (5na/L_0)$ and $|\bar{x}_k - \bar{x}_i|(2 + \epsilon)a$, with $\epsilon = 0.2$ (empirically determined to maximize classification accuracy). Plectoneme loops involve two strands entwined in antiparallel directions (alignment $\to -1$), while segments of adjacent solenoid loops tend to lie parallel (alignment $\to 1$), and straight segments do not contribute to the average. In Fig. 3 we

show four qualitatively different filament configurations: rectilinear, plectoneme, solenoid, and a mixed state with features of both plectonemes and solenoids. Indeed, the distinction between solenoid and plectoneme becomes blurred near the triple point. These simulations agree qualitatively with experimental observations [13], as illustrated in Fig. 3; the small quantitative discrepancy between experiments and simulations is likely due to our neglect of friction. It is worth pointing out that the region of solenoid-plectoneme coexistence can be expanded by having an active agent (for example, a DNA-binding enzyme) capable of either relaxing the internal axial tension and/or inducing excess twist in the filament locally. This allows for the formation of a plectoneme in the compressed segment, after which, upon further twisting, a solenoid forms below the lifted point (Supplemental Material [19] and Fig. S9), with similarities to loop formation in chromosomes [38–40].

Our results also explain earlier observations [12] that describe straight-plectoneme-solenoid transitions in terms of varying twist density and correspond to tracing horizontal and diagonal paths through the present extension-twist density phase diagram (see Supplemental Material [19]). Indeed, horizontally exiting the solenoid region in Fig. 3 to the right, by gradually displacing the lower solenoid end point away from the top leads to a steplike
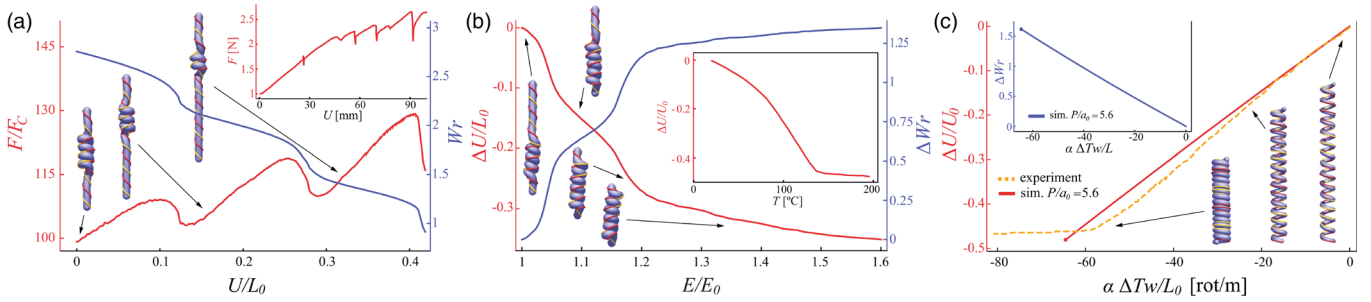
FIG. 4. Actuation of fiber-based artificial muscles that use the straight-solenoid transition. (a) Passive extension via solenoid loss. We displace the unclamped end $\bar{x}_n$ of a solenoid formed as in Fig. 3 with a load $\approx 99 F_C$ a distance ΔU in the direction $\bar{x}_n - \bar{x}_0$ and plot force on $\bar{x}_n$ qualitatively reproducing experiments [13] (inset; see Video S13 in the Supplemental Material [19]). Simulation settings (Supplemental Material): $L_0 = 1$ m, $a = 0.025 L_0$, $E = 1$ MPa, $G = 2E/3$, $S = \mathrm{diag}(4GA/3, 4GA/3, EA)$ N, $B = \mathrm{diag}(EI_1, EI_2, GI_3)$ N m^2. (b) Active work done by changing the temperature, which effectively increases filament rigidity, here simply modeled by increasing the Young's modulus E of the material. This leads to the formation of a solenoidal loop in a stretched twisted filament as in Fig. 3 with a load $\approx 116 F_C$ as E_0 increases gradually from 1 MPa, showing displacement ΔU of $\bar{x}_n$ and increase in writhe $\Delta \mathrm{Wr}$ from initial coil writhe, reproducing experiments [14] (inset; see Video S3 in the Supplemental Material [19]). (c) Contraction of twisted and coiled nylon polymer muscle formed by inserting twist and annealing into a helix. Filament radius doubles from initial radius $a_0 = 0.01$ m, while twist decreases to keep ak_3 constant. Numerical slope and onset of self-contact (shown as a point) agree closely with experimental results [14] (see Supplemental Material [19] for details). Beyond self-contact, radial growth pushes adjacent loops farther apart leading to helix elongation. Note that $\Delta \mathrm{Tw} + \Delta \mathrm{Wr} < 0$ in the inset. Indeed, link escapes from the free boundary due to revolution of the free filament end point around the helix axis, reducing the number of loops in the helix (see Supplemental Material [19] Fig. S7 and Videos S4 and S5). Simulation settings (Supplemental Material [19]): $L_0 = 1$ m, $a = 0.025 L_0$, $E = 30$ GPa, $G = 2E/3$, $S = \mathrm{diag}(4GA/3, 4GA/3, EA)$ N, $B = \mathrm{diag}(EI_1, EI_2, GI_3)$ N m^2. Note that pitch P, $\alpha = 100$, number of loops, and helix radius determine L_0.

solenoid *loss* process. We track the required force and resulting change in writhe [Fig. 4(a)]. The solenoid remains mostly coiled, resisting stretching with a linear-force-displacement relation, until a critical displacement at which it uncoils by one pitch and the process starts again. This stepwise uncoiling stems from a kinematic competition similar to solenoid formation: stretching the filament increases the energy required to maintain a constant number of coils. The simulated sawtooth-force-displacement pattern agrees qualitatively with experiments [13].

Finally, we use our results to quantitatively explain a series of recent experiments on twisted-fiber-based artificial muscles [14,41–43] that exploit the connection between twist, writhe, and link. The fundamental mechanism in each of these studies is associated with the formation of solenoids that this leads to an increase in writhe, causing the filament to shorten and do work against external loads. In the twisted-fiber-based artificial muscles, the externally induced twist is replaced by the use of a scalar field, temperature, that drives variations in the radius and stiffness of a pretwisted filament and causes it to untwist, producing an increase in writhe.

In Fig. 4(b), we simulate this in a minimal setting by showing the effects of (temperature-induced) increase in the elastic modulus of a prestretched, twisted, and loaded filament. To increase writhe, the solenoidal state progressively invades the straight state, lifting its lower end point toward the clamped end, qualitatively reproducing experimental observations of the linear actuator [14]. The sheath-run artificial muscles [41] work similarly by relying on the

conversion of untwist to writhe, while the strain-programmable artificial muscles [42] generate a tensile stroke via temperature-induced differential expansion in a bilayer that is tantamount to changing the natural curvature of a filament dynamically. Finally, the torsional actuator [43] generates torque by inserting twist into a filament and then quickly lowering the filament's intrinsic twist until it vanishes. Rather than replicate all the different variants of the fiber-based artificial muscles, here we limit ourselves to just two simple cases: the linear actuator [14] and the rotary or torsional actuator [43].

To capture the mechanics of the linear actuator, we initialize a filament with intrinsic twist and numerically anneal the filament into a uniform coil with space between adjacent loops, replicating the plastic deformation process by which twisted and coiled polymer muscles are formed. The fibers used in Ref. [14] expand radially and contract axially when heated; however, as noted quantitatively in Ref. [44], considering radial growth with fixed fiber length is sufficient. While our model applies to an isotropic filament, we can simulate anisotropic expansion-driven untwist by following the mechanical analogy in Ref. [14]. Imagine winding an inextensible string around a fiber, attaching it on both fiber ends. To keep the length of the string constant, the fiber would have to untwist to expand. Mathematically, this requires ak_3 to stay constant. Hence, we prescribe a radial growth rate and continuously update the intrinsic twist $\hat{k}_3$ to keep $a\hat{k}_3$ constant [45]. For a homochiral coil, the resulting untwist leads to contraction (Fig. 4), but in a heterochiral coil, untwisting leads to

elongation (Supplemental Material [19] Fig. S8 and Videos S6 and S7). In Fig. 4(c), we show the change in Wr and contraction for a simulated coil with initial nonzero twist density. The coils contract at the same scaled rate as experiments until adjacent loops come into contact (see Supplemental Material [19] for details of varying P/a_0). To capture the mechanics of the rotary actuator [43], we initialize the filament with intrinsic twist which is then rapidly decreased to mimic the effect of annealing via heating leading to rotary motion (see Supplemental Material [19] Sec. S7, Video S14).

Altogether, our study links topology, geometry, and mechanics to explain the complex morphology of soft, strongly stretched, twisted filaments, Additionally, we showed how twist, link and writhe can be interconverted via either external loads or temperature variations, thus allowing us to quantify recent experiments on artificial muscle fibers, setting the stage for the study of complex braided, knotted, and twisted filament configurations in a range of new settings.

[*]lmahadev@g.harvard.edu

[1] G. Kirchhoff, J. Reine. Angew. Math. **56**, 285 (1859).

[2] A. E. H. Love, *A Treatise on the Mathematical Theory of Elasticity* (Cambridge University Press, Cambridge, England, 1892).

[3] S. S. Antman, *Nonlinear Problems of Elasticity* (Springer, New York, 2004).

[4] O. M. O'Reilly, *Modeling Nonlinear Problems in the Mechanics of Strings and Rods: The Role of the Balance Laws* (Springer, New York, 2017).

[5] D. Beard and T. Schlick, J. Chem. Phys. **112**, 7323 (2000).

[6] J. Coyne, IEEE Journal of Oceanic Engineering **15**, 72 (1990).

[7] G. H. M. Van der Heijden and J. M. T. Thompson, Nonlinear Dyn. **21**, 71 (2000).

[8] D. M. Stump, W. B. Fraser, and K. E. Gates, Proc. R. Soc. A **454**, 2123 (1998).

[9] W. K. Olson and P. S. Zhang, Methods Enzymol. **203**, 403 (1991).

[10] J. F. Marko and S. Neukirch, Phys. Rev. E **85**, 011908 (2012).

[11] X. Zhang, F. Chan, T. Parthasarathy, and M. Gazzola, Nat. Commun. **10**, 4825 (2019).

[12] J. W. S. Hearle and A. E. Yegin, J. Text. Inst. **63**, 490 (1972).

[13] A. Ghatak and L. Mahadevan, Phys. Rev. Lett. **95**, 057801 (2005).

[14] C. Haines, N. Li, G. Spinks, A. Aliev, J. Di, and R. Baughman, Proc. Natl. Acad. Sci. U.S.A. **113**, 11709 (2016).

[15] S. H. Kim, C. Haines, N. Li, K. J. Kim, T. J. Mun, C. Choi, J. Di, Y. J. Oh, J. P. Oviedo, J. Bykova *et al.*, Science **357**, 773 (2017).

[16] S. H. Kim, H. J. Sim, J. S. Hyeon, D. Suh, G. M. Spinks, R. Baughman, and S. J. Kim, Sci. Rep. **8**, 8712 (2018).

[17] N. Atikah, L. Y. Weng, A. Anuar, C. C. Fat, I. Z. Abidin, and K. S. M. Sahari, AIP Conf. Proc. **1883**, 020042 (2017).

[18] M. Gazzola, L. Dudte, A. McCormick, and L. Mahadevan, R. Soc. Open Sci. **5**, 171628 (2018).

[19] See Supplemental Material at http://link.aps.org/supplemental/10.1103/PhysRevLett.123.208003 for further discussion of model validity and for more details about the physical model, numerical scheme and representative simulations, which includes Refs. [20–24].

[20] L. R. G. Treloar, Trans. Faraday Soc. **40**, 59 (1944).

[21] S. Reese and P. Wriggers, Comput. Methods Appl. Mech. Eng. **148**, 279 (1997).

[22] O. Ahumada, M. Cocca, G. Gentile, E. Martuscelli, and L. D'Orazio, Textile research Journal : publication of Textile Research Institute, Inc and the Textile Foundation **74**, 1001 (2004).

[23] D. Clark, W. Fleming, R. Bosanquet, and E. Down, Phys. Med. Biol. **41**, 1233 (1996).

[24] O. Rodrigues, Journal de Mathématique Pures et Appliquées **5**, 380 (1840).

[25] J. Spillmann and M. Teschner, *Symposium on Computer Animation: Proceedings of the 2007 ACM SIGGRAPH/ Eurographics Symposium on Computer Animation* (2007).

[26] B. Audoly, N. Clauvelin, P. T. Brun, M. Bergou, E. Grinspun, and M. Wardetzky, J. Comput. Phys. **253**, 18 (2013).

[27] M. Bergou, M. Wardetzky, S. Robinson, B. Audoly, and E. Grinspun, ACM Trans. Graph. **27**, 1 (2008).

[28] F. B. Fuller, Proc. Natl. Acad. Sci. U.S.A. **75**, 3557 (1978).

[29] G. Calugareanu, Rev. Math. Pures Appl **4**, 5 (1959).

[30] R. Ricca and B. Nipoti, J. Knot Theory Ramif. **20**, 1325 (2011).

[31] F. B. Fuller, Proc. Natl. Acad. Sci. U.S.A. **68**, 815 (1971).

[32] K. Klenin and J. Langowski, Biopolymers **54**, 307 (2000).

[33] S. Gerbode, J. Puzey, A. McCormick, and L. Mahadevan, Science **337**, 1087 (2012).

[34] A. R. Champneys, G. H. M. Van der Heijden, and J. M. T. Thompson, SIAM J. Appl. Math. **59**, 198 (1998).

[35] A. Goriely and M. Tabor, Phys. Rev. Lett. **80**, 1564 (1998).

[36] J. D. Moroz and P. Nelson, Proc. Natl. Acad. Sci. U.S.A. **94**, 14418 (1997).

[37] A. Majumdar and A. Raisch, Nonlinearity **27**, 2841 (2014).

[38] G. Fudenberg, M. Imakaev, C. Lu, A. Goloborodko, N. Abdennur, and L. Mirny, Cell Rep. **15**, 2038 (2016).

[39] M. Ganji, I. A. Shaltiel, S. Bisht, E. Kim, A. Kalichava, C. H. Haering, and C. Dekker, Science **360**, 102 (2018).

[40] B. Soh, V. Narsimhan, A. R. Klotz, and P. S. Doyle, Soft Matter **14**, 1689 (2018).

[41] J. Mu *et al.*, Science **365**, 150 (2019).

[42] M. Kanik *et al.*, Science **365**, 145 (2019).

[43] J. Yuan, W. Neri, C. Zakri, P. Merzeau, K. Kratz, A. Lendlein, and P. Poulin, Science **365**, 155 (2019).

[44] C. Lamuta, S. Messelot, and S. Tawfick, Smart Mater. Struct. **27**, 055018 (2018).

[45] Note that we update *intrinsic* twist (twist of the filament in its rest configuration) $\widehat{k}_3$ rather than true twist k_3, since k_3 must evolve according to the equations of motion. The filament twisting strain is defined by $k_3 - \widehat{k}_3$, so the filament deforms to try to make $k_3 = \widehat{k}_3$. After the onset of self-contact, radial growth pushes adjacent loops apart, lowering filament writhe and thereby forcing the filament to retwist despite an ever-increasing intrinsic twist.